ORIGINAL PAPER

Comparison of optimization parametrizations for regional lung compliance estimation using personalized pulmonary poromechanical modeling

Colin Laville[1,2] · Catalin Fetita[3] · Thomas Gille[4,5] · Pierre-Yves Brillet[4,5] · Hilario Nunes[4,5] · Jean-François Bernaudin[4] · Martin Genet[1,2]

Abstract

Interstitial lung diseases, such as idiopathic pulmonary fibrosis (IPF) or post-COVID-19 pulmonary fibrosis, are progressive and severe diseases characterized by an irreversible scarring of interstitial tissues that affects lung function. Despite many efforts, these diseases remain poorly understood and poorly treated. In this paper, we propose an automated method for the estimation of personalized regional lung compliances based on a poromechanical model of the lung. The model is personalized by integrating routine clinical imaging data – namely computed tomography images taken at two breathing levels in order to reproduce the breathing kinematic—notably through an inverse problem with fully personalized boundary conditions that is solved to estimate patient-specific regional lung compliances. A new parametrization of the inverse problem is introduced in this paper, based on the combined estimation of a personalized breathing pressure in addition to material parameters, improving the robustness and consistency of estimation results. The method is applied to three IPF patients and one post-COVID-19 patient. This personalized model could help better understand the role of mechanics in pulmonary remodeling due to fibrosis; moreover, patient-specific regional lung compliances could be used as an objective and quantitative biomarker for improved diagnosis and treatment follow up for various interstitial lung diseases.

Keywords Pulmonary mechanics · Poromechanics · Finite element method · Image-based estimation · Optimization

1 Introduction

Idiopathic pulmonary fibrosis (IPF) is still today a poorly understood disease, characterized by the thickening and stiffening of lung interstitial tissues (Nunes et al. 2015, Plantier et al. 2018). It is a severe chronic disease leading to progressive and irreversible deterioration of lung function due to impaired gas exchange, with very few available treatments (Flaherty et al. 2018). As the disease progresses, patients suffer from persistent and increasing symptoms of dyspnea, dry cough, chest pain, fatigue, *etc.* (Flaherty et al. 2018).

More recently, post-COVID-19 pulmonary fibrosis has been frequently reported (George et al. 2020, Giacomelli et al. 2021). About 8% of patients present severe lung

✉ Martin Genet
  martin.genet@polytechnique.edu

  Colin Laville
  colin.laville@polytechnique.edu

  Catalin Fetita
  catalin.fetita@telecom-sudparis.eu

  Thomas Gille
  thomas.gille@aphp.fr

  Pierre-Yves Brillet
  pierre-yves.brillet@aphp.fr

  Hilario Nunes
  hilario.nunes@aphp.fr

  Jean-François Bernaudin
  jean-francois.bernaudin@sorbonne-universite.fr

[1] Laboratoire de Mécanique des Solides, École Polytechnique/CNRS/IPP, Palaiseau, France

[2] Inria, Palaiseau, France

[3] SAMOVAR, Télécom SudParis/IMT/IPP, Évry, France

[4] Hypoxie et Poumon, Université Sorbonne Paris Nord/INSERM, Bobigny, France

[5] Hôpital Avicenne, APHP, Bobigny, France

capacity impairment, chest pain, painful muscles, ageusia, anosmia or fibrotic damage that could be attributed to the COVID-19 infection (Ballering et al. 2022). The severity of the initial symptoms is correlated with a higher risk of persistent respiratory complications (McGroder et al. 2021). These long-term complications may cause substantial patients disability and even death due to lung fibrosis progression in the following years, and thus drastically increase pulmonary fibrosis prevalence (Michalski et al. 2022).

Like in other clinical fields (Smith et al. 2011, Lee et al. 2014), patient-specific numerical models are intended to play a role in such clinical issues, through individualized diagnosis, prognosis and long term follow up, evaluating effectiveness of a treatment over time from a mechanical point of view (Roth et al. 2017, Morton et al. 2018). Moreover, they could give additional information to clinicians in order to propose individualized therapies. Regarding post-COVID-19 patients, these models may help for early detection of pulmonary fibrosis.

Pulmonary fibrosis is also associated to more fundamental issues. For instance, the underlying mechanisms involved in progression and worsening over time are not fully understood. One of the hypotheses is the existence of a mechanical vicious circle (Liu et al. 2010, Carloni et al. 2013, Wu et al. 2020). According to this assumption, the thickening of the interstitial tissues due to pulmonary fibrosis locally increases its rigidity inducing higher stresses, which activates the production of collagen fibers by fibroblasts in the surrounding area (Liu et al. 2015). Only a few studies have tried to evaluate this hypothesis. A possible investigative approach, that we will sustain in this paper, is through personalized biomechanical modeling of fibrotic lungs based on medical imaging.

Numerical modeling of lungs, and especially finite-element modeling, have been widely used in the literature to study air flow and gas exchange (Neelakantan et al. 2022). At a more general level including mechanical deformation and fluid-solid interaction, it is an active research field that aims to understand the biomechanics of the lung and its function under normal and pathological conditions, both through a micromechanical approach (Knudsen and Ochs 2018, Concha et al. 2018, Sarabia-Vallejos et al. 2019) or at the organ level (Berger et al. 2016, Roth et al. 2017, Avilés-Rojas and Hurtado xxx), and through multiphysics and multiscale approaches (Wall et al. 2010, Leonard-Duke et al. 2020). Several authors have demonstrated the need of using heterogeneous mechanical behavior for lung tissue modeling. One can refer for instance to Arora et al. (2021), Mariano et al. (2022), that performed *ex-vivo* 3D digital image correlation or digital volume correlation deformation measurements of inflated lungs at organ level. Thus, various constitutive laws have been considered

for the parenchyma either or not based on microstructure or experimental measurements (Birzle and Wall 2019, Birzle et al. 2019).

In this context, a lung biomechanical model was recently proposed in Patte et al. (2022) based on a general poromechanical formulation in large strains (Biot and Temple 1972, Chapelle et al. 2010, Chapelle and Moireau 2014). The model uses a two-phase mixture theory under the assumption of fluid incompressibility and isothermal conditions. The fluid phase represents air in the alveoli, while the solid phase represents tissues and blood, and is modeled with an hyperelastic free energy potential suitable for biological soft tissues such as lung parenchyma. The boundary conditions for breathing modeling, already detailed in Patte et al. (2022), are a negative pleural pressure applied on the external surface of the lungs and a frictionless bilateral contact with the thorax. The model is associated to a personalization pipeline, introduced in Patte et al. (2022), which allows to generate patient-specific models based on clinical images, and thus to obtain biomarkers combining the laws of physics and acquired data, opening the door for a better understanding, diagnosis and treatment of pulmonary fibrosis.

The work presented in this paper focuses on improving the lung model personalization pipeline based on clinical data presented in Patte et al. (2022), for the estimation of patients regional lung compliances. Segmentation and meshing steps were improved and automated. The method relies on two 3DCT images for each patient, taken at end-exhalation and end-inhalation (breath holding), which are routinely acquired on patients diagnosed with pulmonary fibrosis, either IPF or post-COVID-19, at Avicenne APHP Hospital, Bobigny, France. Patient-specific information, such as lungs and thorax geometry, breathing kinematics, local porosity and fibrotic regions are extracted from the images. The image registration step, from which breathing kinematics is derived, was made more robust through a multi-level (rigid body, affine and full motion) decomposition. Then, regional lung compliances are estimated through an inverse problem. Since pleural pressure cannot be measured in clinical routine, a generic pleural pressure was used for all patients in Patte et al. (2022), leading in some cases to inconsistent estimation results. In this paper, we assess this major drawback by introducing a new parametrization based on the estimation of a personalized pleural pressure in addition to material parameters, allowing the use of fully patient-specific boundary conditions for the inverse problem. Results on IPF patients are compared to previous work (Patte et al. 2022), and results on post-COVID-19 are presented for the first time.

2 Materials and methods

2.1 Thoracic imaging

The personalized poromechanical modeling tools presented in this paper are based on patient-specific clinical data such as lung geometry, lung porosity and breathing kinematics, which are obtained from clinical imaging. CT scans are usually used for interstitial lung diseases (Hartley et al. 1994, Washko et al. 2011) and are routinely performed for the diagnosis, classification and long-term followup at Avicenne APHP Hospital, Bobigny, France. Two high resolution 3DCT scans were performed on each patient, at end-exhalation and end-inhalation, in the supine position with the arms above the head and in breath-hold during image acquisition, following French guidelines (Cottin et al. 2014). Visual image analysis and classification were done by a radiologist.

In this study, 3DCT scans of three IPF patients and one post-COVID-19 patient were selected. The CT parameters used for acquisition and reconstruction are given in Table 1. Patient data were retrospectively retrieved according to the French law on medical research and compiled as required by the *Commission Nationale de l'Informatique et des Libertés* (CNIL). The study not requiring an informed consent received authorization CLEA-2019-96 from the *Comité Local d'éthique d'Avicenne* (CLEA).

2.2 Recall on lung poromechanical modeling

2.2.1 General modeling assumptions

As a general reminder, poromechanical modeling is intended to capture the heterogeneous mechanical behavior of the lung at organ level due to the incorporation of microscopic information, such as local porosity. In this model, the lung parenchyma was considered as a two-phase poroelastic continuum. We used a general large strain mixture theory presented in Chapelle and Moreau (2014) and applied to lung modeling in Patte et al. (2022). The solid phase regroups

lung interstitial tissue and blood, and the fluid phase corresponds to air present in airways and alveoli. Both solid and fluid phases were considered as incompressible under normal breathing conditions, so that lung volume change is due to added and removed fluid phase to the mixture, respectively, with inhalation and exhalation. Thus, the model relies on lung local porosity information in the reference configuration, representing the volume fraction of air. Moreover, the following additional hypotheses were made:

- The transformation is assumed to be isothermal.
- End-exhalation and end-inhalation states were considered at static equilibrium.
- Internal fluid pressure is homogeneous and equal to atmospheric pressure.
- The existence of an unknown unloaded configuration at equilibrium corresponding to a null pleural pressure.
- The end-exhalation pleural pressure was set to a normal value of -0.5 kPa.

2.2.2 Poromechanical framework

We define the following kinematic mapping between the reference configuration, denoted Ω_0, and the deformed configuration, denoted ω:

$$\underline{\chi} := \begin{cases} \Omega_0 \rightarrow \omega \\ \underline{X} \mapsto \underline{x} = \underline{\chi}(\underline{X}). \end{cases} \tag{1}$$

The corresponding deformation gradient is

$$\underline{\underline{F}}(\underline{X}) := \underline{\underline{\nabla}}\, \underline{\chi} = \underline{\underline{1}} + \underline{\underline{\nabla}}\, \underline{U}, \tag{2}$$

where the displacement field is

$$\underline{U}(\underline{X}) := \underline{\chi}(\underline{X}) - \underline{X} = \underline{x}(\underline{X}) - \underline{X}. \tag{3}$$

The associated local volume change of the mixture is

$$J := \det\left(\underline{\underline{F}}\right) = \Phi_s + \Phi_f, \tag{4}$$

Table 1 Acquisition and reconstruction CT parameters for each patient

CT parameters	Patients			
	IPF1	IPF2	IPF3	COVID1
Manufacturer	Siemens	Siemens	Siemens	GE
Model	Somatom	Somatom	Somatom	Revolution HD
KVP	120	120	120	120
Convolution kernel	I70f/4	I70f/4	I70f/4	LUNG
Columns	512	512	512	611
Rows	512	512	512	611
Axial pixel spacing [mm]	0.66	0.7	0.68	0.6
Slice thickness [mm]	0.75	0.75	0.75	0.6

with Φ_s and Φ_f, respectively, the solid and fluid contributions to the mixture volume change. Moreover, we have

$$\begin{cases} \Phi_f = \phi_f \cdot J \\ \Phi_s = \phi_s \cdot J = (1 - \phi_f) \cdot J \end{cases},$$ (5)

where ϕ_s and ϕ_f are, respectively, the solid and fluid volume fraction in the deformed configuration. Thus, we have, in the reference configuration Ω_0, $\Phi_{f0} + \Phi_{s0} = 1$, and, in the deformed configuration ω, $\phi_f + \phi_s = 1$.

We also introduce the right Cauchy-Green deformation tensor

$$\underline{\underline{C}} := \underline{\underline{F}}^T \cdot \underline{\underline{F}},$$ (6)

and its first three invariants:

$$\begin{cases} I_1 := \mathrm{tr}\left(\underline{\underline{C}}\right) \\ I_2 := \frac{1}{2}\left(\mathrm{tr}\left(\underline{\underline{C}}\right)^2 - \mathrm{tr}\left(\underline{\underline{C}}^2\right)\right) \\ I_3 := \det\left(\underline{\underline{C}}\right) = J^2 \end{cases}.$$ (7)

The Green-Lagrange strain tensor is denoted by

$$\underline{\underline{E}} := \frac{1}{2}\left(\underline{\underline{C}} - \underline{\underline{1}}\right).$$ (8)

In addition to these kinematics variables, another variable is needed to characterize the fluid transport within the mixture. Thus, we define the fluid mass change per unit reference mixture volume, denoted $\overline{\rho}_{f\pm}$. Using the fluid incompressibility assumption, we have:

$$\overline{\rho}_{f\pm} = \rho_{f0} \cdot \left(\Phi_f - \Phi_{f0}\right),$$ (9)

with ρ_{f0} the reference fluid mass density.

2.2.3 Poromechanical equilibrium laws

The weak form of the balance of linear momentum in the current and reference configurations are, respectively:

$$\int_\omega \underline{\underline{\sigma}} : \underline{\underline{\varepsilon}}\left(\underline{u}^*\right) \mathrm{d}\omega = W_{ext}\left(\underline{u}^*\right) \quad \forall \underline{u}^*,$$ (10)

and

$$\int_{\Omega_0} \underline{\underline{\Sigma}} : \mathrm{d}_{\underline{U}}\underline{\underline{E}} \cdot \underline{U}^* \mathrm{d}\Omega_0 = W_{ext}\left(\underline{U}^*\right) \quad \forall \underline{U}^*,$$ (11)

where $\underline{\underline{\sigma}}$ and $\underline{\underline{\Sigma}}$ are the Cauchy and second Piola-Kirchhoff stress tensors. $\underline{\underline{\varepsilon}}\left(\underline{u}^*\right)$ is the linearized strain tensor, $\mathrm{d}_{\underline{U}}\underline{\underline{E}} \cdot \underline{U}^*$ is the differential of the Green-Lagrange strain tensor and W_{ext} is the virtual work of the external forces that will be detailed in Sect. 2.2.5. We also consider the local mixture

equilibrium between the fluid pressure p_f and the solid hydrostatic pressure p_s (formally defined in the next paragraph) such that

$$p_f = p_s.$$ (12)

2.2.4 Poromechanical constitutive law

Following the second principle of thermodynamics, the second Piola-Kirchhoff stress tensor derives from a Helmholtz free energy function of the mixture, denoted $\overline{\psi}$, with respect to E. $\overline{\psi}$ is decomposed additively into a solid part $\overline{\psi}_s$ and a fluid part $\overline{\psi}_f$:

$$\overline{\psi}\left(\underline{\underline{E}}, \overline{\rho}_{f\pm}\right) = \overline{\psi}_s\left(\underline{\underline{E}}, \Phi_s\right) + \overline{\psi}_f\left(\Phi_f\right).$$ (13)

Thus,

$$\underline{\underline{\Sigma}} = \frac{\partial \overline{\psi}\left(\underline{\underline{E}}, \overline{\rho}_{f\pm}\right)}{\partial \underline{\underline{E}}} = \frac{\partial \overline{\psi}_s}{\partial \underline{\underline{E}}} - p_s J \underline{\underline{C}}^{-1},$$ (14)

where the solid hydrostatic pressure $p_s := -\dfrac{\partial \overline{\psi}_s}{\partial \Phi_s}$ is related to the volume change.

The free energy function associated with the solid mechanical behavior is decomposed following:

$$\overline{\psi}_s\left(\underline{\underline{E}}, \Phi_s\right) = \overline{W}_{skel}\left(\underline{\underline{E}}\right) + \overline{W}_{bulk}\left(\Phi_s\right)$$ (15)

where the first term $\overline{W}_{skel}$ accounts for the solid structure behavior and the second term $\overline{W}_{bulk}$ stems from the compressibility of the solid phase. According to Patte et al. (2022, 2022), the hyperelastic response of the lung tissues may then be represented using the following strain-energy functions:

$$\begin{cases} \overline{W}_{skel}\left(\underline{\underline{E}}\right) = \overline{\alpha}\left(e^{\delta\left(J^2 - 1 - 2\ln(J)\right)} - 1\right) \\ \qquad + \overline{\beta}_1\left(I_1 - 3 - 2\ln(J)\right) + \overline{\beta}_2\left(I_2 - 3 - 4\ln(J)\right), \\ \overline{W}_{bulk}\left(\Phi_s\right) = \overline{\kappa}\left(\frac{\Phi_s}{\Phi_{s0}} - 1 - \ln\left(\frac{\Phi_s}{\Phi_{s0}}\right)\right) \end{cases}$$ (16)

where $\overline{\alpha}, \overline{\beta}_1, \overline{\beta}_2, \delta$ are material parameters and $\overline{\kappa}$ is the solid bulk modulus which should be large enough to ensure quasi-incompressibility of the solid part. These parameters $\overline{\theta}$ represent the effective behavior of the mixture, intrinsically taking into account the local reference porosity such that:

$$\overline{\theta} = \left(1 - \Phi_{f0}\right)\theta = \Phi_{s0}\theta \quad \forall \overline{\theta} \in \{\overline{\alpha}, \overline{\beta}_1, \overline{\beta}_2, \overline{\kappa}\}.$$ (17)

One can note that homogeneous material parameters weighted with the local reference porosity can produce highly heterogeneous effective poromechanical behavior, depending on the heterogeneity of the porosity field, which is needed for the lung parenchyma (Maghsoudi-Ganjeh et al. 2021).

2.2.5 Lung model

As presented in Patte et al. (2022), since the initial configuration at end-exhalation is not stress free, the first step is to compute an unloaded configuration corresponding to a null pleural pressure. This is an inverse problem in which the initial porosity corresponding to the loaded end-exhalation configuration, denoted γ_e, is known. The only initial boundary condition is an homogeneous negative pleural pressure $p_{\mathrm{pl,e}}$, set to -0.5 kPa on the whole lung surface, while rigid body motion are blocked. The two unknowns are the inverse displacement $\underline{u}_0$ and the reference porosity Φ_{f0}. The weak form of the problem is:

Find $\left(\underline{u}_0, \phi_{\mathrm{f0}}\right)$ such that

$$\begin{cases} \forall \underline{u}^*, \ \int_{\omega_e} \underline{\underline{\sigma}}(\underline{u}_0, \phi_{\mathrm{f0}}) : \underline{\underline{\varepsilon}}(\underline{u}^*)\mathrm{d}\omega = -\int_{\gamma_e} p_{\mathrm{pl,e}} \, \underline{n} \cdot \underline{u}^*\mathrm{d}\gamma \\ \forall \underline{x}, \ p_{\mathrm{f}} = -\dfrac{\partial \overline{W}_{\mathrm{bulk}}}{\partial \Phi_{\mathrm{s}}}(\underline{u}_0, \phi_{\mathrm{f0}}) \end{cases} \quad (18)$$

where $\phi_{\mathrm{f0}} = \Phi_{\mathrm{f0}} \circ \underline{\chi}_0^{-1} J^{-1}$ using the inverse mapping $\underline{\chi}_0^{-1}$. The model boundary conditions and some poromechanical quantities are illustrated in Fig. 1, where we used the multiplicative decomposition of the global deformation gradient as follow:

$$\underline{\underline{F}} = \underline{\underline{F}}_b \cdot \underline{\underline{F}}_0. \quad (19)$$

After the resolution of the inverse problem, the pre-stressed end-exhalation configuration at equilibrium is fully known. The loading towards the end-inhalation configuration involves much more complex boundary conditions. In addition to the negative pleural pressure on the whole lung surface, a bilateral sliding contact with no friction and no separation, is set between the lung and the thorax surface. The problem is then described by the following system of equations:

Find $\left(\underline{U}, \Phi_{\mathrm{f}}\right)$ such that

$$\begin{cases} \forall \underline{U}^*, \ \int_{\Omega_0} \dfrac{\partial \overline{W}_{\mathrm{skel}}}{\partial \underline{\underline{E}}} : \mathrm{d}_{\underline{U}}\underline{\underline{E}} \cdot \underline{U}^*\mathrm{d}\Omega_0 - \int_{\Omega_0} p_{\mathrm{f}} J \underline{\underline{C}}^{-1} : \mathrm{d}_{\underline{U}}\underline{\underline{E}} \cdot \underline{U}^*\mathrm{d}\Omega_0 \\ = -\int_{\Gamma_0} p_{\mathrm{pl}} J\left(\underline{\underline{F}}^{-T} \cdot \underline{N}_0\right) \cdot \underline{U}^*\mathrm{d}\Gamma_0 \\ \forall \underline{X}, \ p_{\mathrm{f}} = -\dfrac{\partial \overline{W}_{\mathrm{bulk}}}{\partial \Phi_{\mathrm{s}}} \end{cases}$$

$$(20)$$

2.3 Model personalization procedure

Figure 2 illustrates the required patients data, *i.e.*, clinical images and segmentation in green, and the fully automated pipeline for the personalized estimation of regional lung compliance in blue.

2.3.1 Images segmentation

The 3DCT images at end-exhalation and end-inhalation are, respectively, denoted I_e and I_i. From these images, lungs and thorax geometries are segmented, where the thorax designates the volume composed of both lungs and the mediastinum. For each lung, an healthy and a diseased region are distinguished in the end-exhalation image I_e.

Fig. 1 Schematic representation of the main poromechanical quantities and model boundary conditions. From left to right, unloaded configuration, initial end-exhalation configuration and loaded end-inhalation configuration
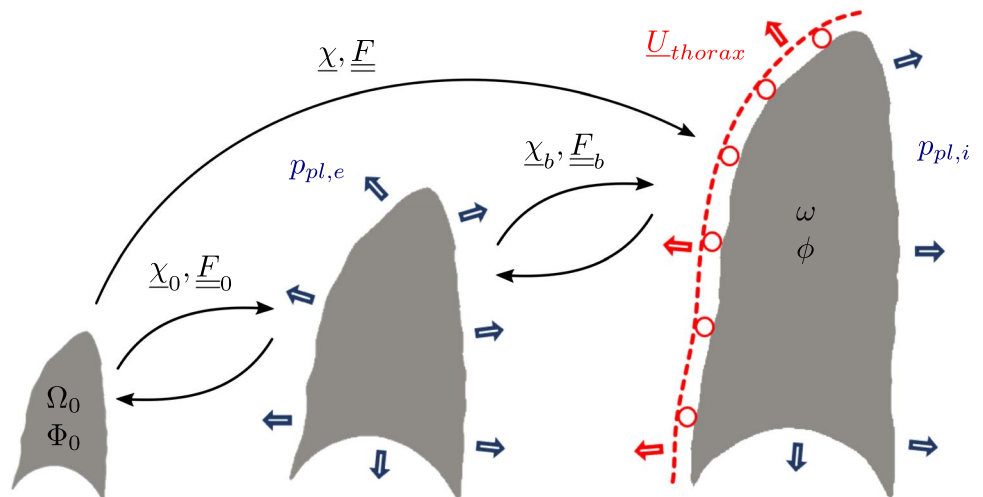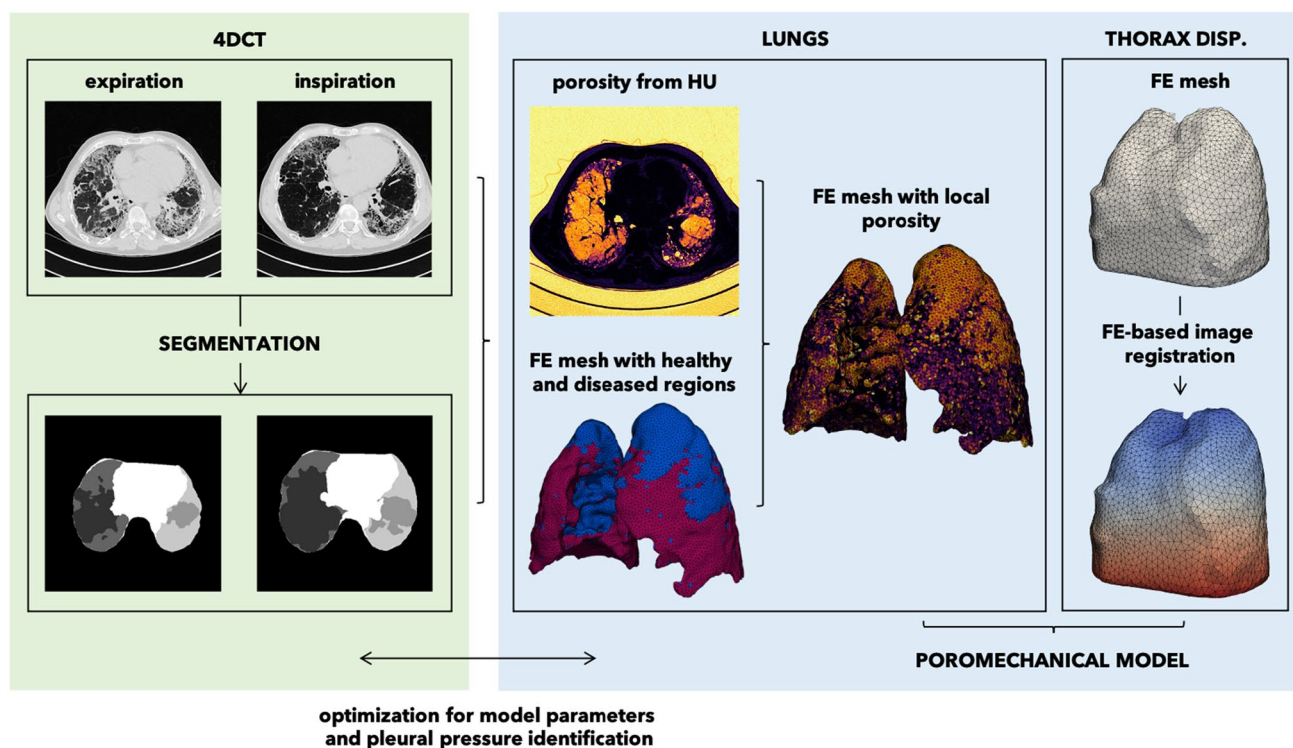
Fig. 2 Schematic representation of the personalized lung modeling pipeline with the required clinical data in green and the automated computational pipeline in blue

The lung segmentation is performed using a U-Net convolutional neural network specialized in the texture classification of fibrotic lungs (Rennotte et al. 2020). A Dice loss function was selected for network training. The learning optimizer used a stochastic gradient with momentum and considered a learning rate which varied with time according to a triangular learning cycle schedule (Smith 2017; Ronneberger et al. 2015). The database used for training and testing the convolutional neural network model was collected at Avicenne Hospital, Bobigny, France. The database included 156 patients totaling 2266 axial images. Among them, 137 patients (2076 slices) are used for train and validation and 19 patients (190 slices) for test. The ground truth annotations were performed manually by an expert radiologist using an in-house software. The segmentation algorithm provides healthy and diseased lung regions, the latter differentiating between fibrosis, ground glass and emphysema patterns. For all our study cases, the segmentation results were validated by an expert radiologist. Based on the lung segmentation, the thorax region was computed as the convex-hull volume encompassing the lungs and the mediastinum, extended in the cranio-caudal direction down to the lung basis. Such task automation

is an important improvement with respect to our previous work (Patte et al. 2022) where lung healthy/diseased regions and thorax volume were defined manually based on lung shape segmentation (Rennotte et al. 2020). Note that the diseased region includes all anomalies related to fibrosis such as scar tissues, ground-glass opacities, honeycombing, *etc.* (Fetita et al. 2016).

2.3.2 Mesh generation

The segmented image slices are combined into a 3D image using the Visualization Toolkit (VTK) (Schroeder et al. 2006) for both end-exhalation and end-inhalation states. From the 3D images, the left lung, right lung and thorax are separately meshed. In previous work (Patte et al. 2022), the healthy and diseased regions segmentation of each lung was a binary field projected onto the finite element mesh, which did not explicitly represent the healthy-diseased interface. One of the improvements introduced in this paper is the explicit meshing of the healthy and diseased regions interface, directly from the automatic segmentation introduced above, using the Computational Geometry Algorithms Library (CGAL) (Project 2022).

Table 2 Model parameters used in simulations for imposed $p_{pl,i}$ and imposed $\overline{\alpha}_h$ estimations

Parameters		Imposed $p_{pl,i}$		Imposed $\overline{\alpha}_h$	
		Healthy	Diseased	Healthy	Diseased
$\overline{\alpha}$	[kPa]	–	–	0.0275	–
$\overline{\beta}_1$	[kPa]	0.2	0.2	0.2	0.2
$\overline{\beta}_2$	[kPa]	0.4	0.4	0.4	0.4
δ	[–]	0.5	0.5	0.5	0.5
p_f	[kPa]	0		0	
$p_{pl,e}$	[kPa]	−0.5		−0.5	
$p_{pl,i}$	[kPa]	−1.85		–	

The 3D mesh generation tool from CGAL allows the generation of an isotropic mesh composed of multiple components or subdomains, here the two lung regions, with a coherent mesh interface. Linear tetrahedron is used.

2.3.3 Porosity projection

The porosity field is then computed from the CT images, which measure the attenuation of X-rays in the tissue related to density. Thus, each image pixel is displayed according to the mean attenuation of the tissue formulated in the Hounsfield units (HU) scale. Assuming a linear variation of porosity with HU, the local porosity can be computed with the expression:

$$\phi_f(\underline{x}) = \frac{HU(\underline{x}) - HU_{\text{tissue}}}{HU_{\text{air}} - HU_{\text{tissue}}}, \tag{21}$$

with $HU_{\text{tissue}} = 0\,\text{HU}$ considering that biological tissues are mainly composed of water and $HU_{\text{air}} = -1000\,\text{HU}$. The porosity field computed from the end-exhalation image is projected onto the corresponding finite element mesh, assuming a constant value on each element. This value is equal to the mean of pixel values for all pixels inside the element.

2.3.4 Image registration

From the meshes of lungs and thorax, new binary masks are created using VTK tools, respectively $M_{l,e}$ and $M_{l,i}$ from empty 3D images of dimensions corresponding to I_e and I_i.

The displacement field of the thorax between end-exhalation and end-inhalation is computed using finite element-based image registration. The method is described in (Genet et al. 2018), and the code is freely available at https://gitlab.inria.fr/mgenet/dolfin_warp.

In our case, the registration problem involves the end-exhalation thoracic mesh and the $M_{l,e}$ and $M_{l,i}$ thoracic binary masks. Since the image registration problem of shapes is ill-posed (Vishnevskiy et al. 2017), a very small hyperelastic regularization term is used to prevent convergence issues. Moreover, to improve the robustness of the registration, which is especially difficult as thorax displacements during breathing can be very large (several centimeters), we introduce here an multi-level registration algorithm:

1. First a rigid body displacement field $\underline{U}_{\text{rb}}$ is computed.
2. From $\underline{U}_{\text{rb}}$ as initial solution, an affine displacement field $\underline{U}_{\text{affine}}$ then is computed.
3. Finally the thorax displacement finite element field $\underline{U}_{\text{thorax}}$ is computed using $\underline{U}_{\text{affine}}$ as initial solution.

The external surface of the volumetric thoracic mesh is then extracted with the corresponding nodal displacements and converted into shell elements.

2.3.5 Model parameters estimation

Patient-specific mechanical parameters of the skeleton energy $\overline{W}_{\text{skel}}$ are estimated using the above data. In this study we consider lungs with two regions, healthy and fibrotic tissues. Each region is defined as sets of elements with homogeneous material model properties. Two kinds of estimation are performed:

1. Identification of the material parameters for both regions imposing a generic end-inhalation pleural pressure $p_{pl,i}$ as already presented in Patte et al. (2022).
2. Identification of the diseased region material parameters $\overline{\Theta}_d$ and end-inhalation pleural pressure $p_{pl,i}$ imposing a generic healthy region material parameter $\overline{\Theta}_h$.

However, the estimation problem of four parameters with the small amount of data available is highly ill-posed. Consequently, only the main volumetric stiffness parameters $\overline{\Theta}_{h/d} = \left\{ \overline{\alpha}_{h/d} \right\}$, are estimated and the others are set as presented in Table 2.

The estimation problem is formulated as an optimization problem, in which the solution is the set of parameters minimizing a cost function f, characterizing the distance between the model and the data and defined in the next paragraph. The optimization process is solved using the stochastic derivative-free numerical optimization algorithm CMA-ES (Auger and Hansen 2005; Hansen 2016), which evaluates the direct problem multiple times with different sets of parameters. Thus, for each CMA-ES evaluation the direct problem consists in computing the stress-free reference configuration from the end-exhalation configuration and the loaded end-inhalation configuration from the reference configuration. The stress-free reference configuration is computed using the FEniCS library (Aln et al. 2015) to solve the inverse hyperelastic problem (18) (code is freely available at https://gitlab.inria.fr/mgenet/dolfin_mech), while the loaded configuration is computed solving (20) using the Abaqus/Standard finite-element solver (ABAQUS 2009).

As detailed in Patte et al. (2022), the cost function used in the optimization process is additively composed of two terms. The first one characterizes the discrepancy between the end-exhalation and end-inhalation images after mapping with the model, while the second term characterizes the discrepancy between the measured (from the images) and predicted (from the model) lung shape changes. In the sum, the weights are chosen such that both terms have an equivalent order of magnitude in the optimal state.

2.4 Regional compliance definition

In order to quantify the regional softness of the lung tissues, independently from the constitutive behavior and the patient-specific lung geometry, we define a global compliance $C_{t_0 \to t_1}$ between two time points t_0 and t_1. It is defined as a volume change divided by a pressure change, such that:

$$C_{t_0 \to t_1} = \frac{V_{t_1} - V_{t_0}}{p_{pl,t_1} - p_{pl,t_0}}, \quad (22)$$

where V_{t_0} and p_{pl,t_0} are, respectively, the lung volume and pleural pressure at time point t_0, and V_{t_1} and p_{pl,t_1} are the lung volume and pleural pressure at time point t_1. In order to define the compliance independently from the patient, we take $V_{t_0} = 1.3$ L and $p_{pl,t_0} = -0.5$ kPa for all patients, and compute V_{t_1} on a simple Rivlin cube simulation.

3 Results

In this section, we present results of the identification. As described in Sect. 2.3.5, two kinds of identification are performed based on clinical data: either by imposing a generic end-inhalation pleural pressure, or by imposing a generic healthy compliance. Results are given in Table 3.

3.1 Parameters identification

We first reproduced identifications performed in Patte et al. (2022) on patients IPF1, IPF2 and IPF3, with the improved and fully automated personalization pipeline. In these computations the end-inhalation pleural pressure is set to $p_{pl,i} = -1.85$ kPa for all patients and regional material parameters $\overline{\alpha}_h$ and $\overline{\alpha}_d$ are estimated. Results are presented in Table 3 and are qualitatively consistent with the identification of Patte et al. (2022).

In order to address some of the limitations of the previous estimation, especially reduce the sensitivity to the quality of the clinical data such as large variability in patients breath, we propose to no longer impose the end-inhalation pleural pressure, and instead impose the lung healthy region stiffness ($\overline{\alpha}_h = 0.0275$ kPa) for all patients (see Table 2). Results are presented in Table 3.

3.2 Clinical analysis

3.2.1 Regional compliance

If global pulmonary compliance is a frequently used biomarker for clinicians that need to quantify impact and severity of pulmonary fibrosis, regional compliance as presented in this article is not yet used in clinical routine. The method used for the computation of the compliance is

Table 3 Comparison of the identified parameters for both kind of estimation, imposed $p_{pl,i}$ and imposed $\overline{\alpha}_h$

Patients	Imposed $p_{pl,i}$		Imposed $\overline{\alpha}_h$	
	$\overline{\alpha}_h$ [kPa]	$\overline{\alpha}_d$ [kPa]	$\overline{\alpha}_d$ [kPa]	$p_{pl,i}$ [kPa]
IPF1	0.021	0.199	5.532	−3.405
IPF2	27.42	1.682	5.753	−0.925
IPF3	0.005	3.859	6.634	−6.727
COVID1	0.006	0.021	3.252	−2.082

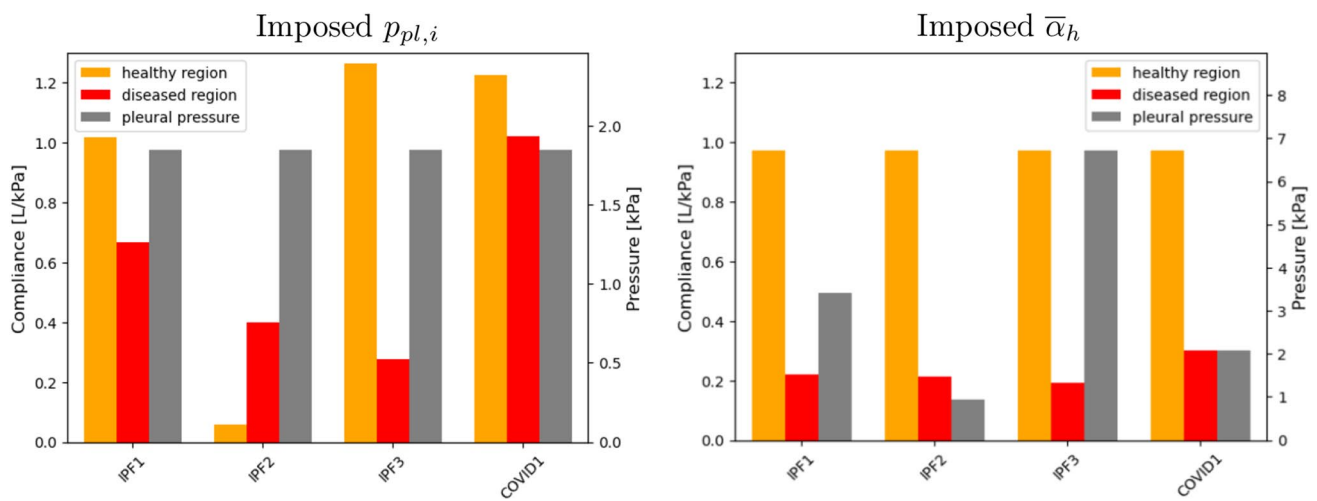**Fig. 3** Regional compliances and pleural pressure for each patient for both estimations, with imposed $p_{pl,i}$ (left) and with imposed $\overline{\alpha}_h$ (right)
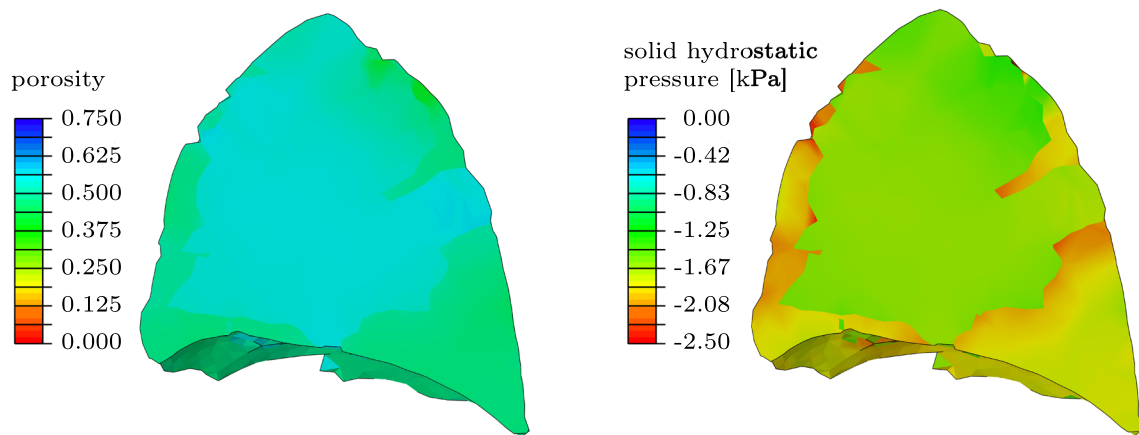

Fig. 4 Comparison of fluid fraction of the mixture (left) and the solid hydrostatic pressure [kPa] (right) in a sagittal slice of the lung for patient IPF1 in the case of a non-patient specific pleural pressure estimation (imposed $p_{pl,i}$)
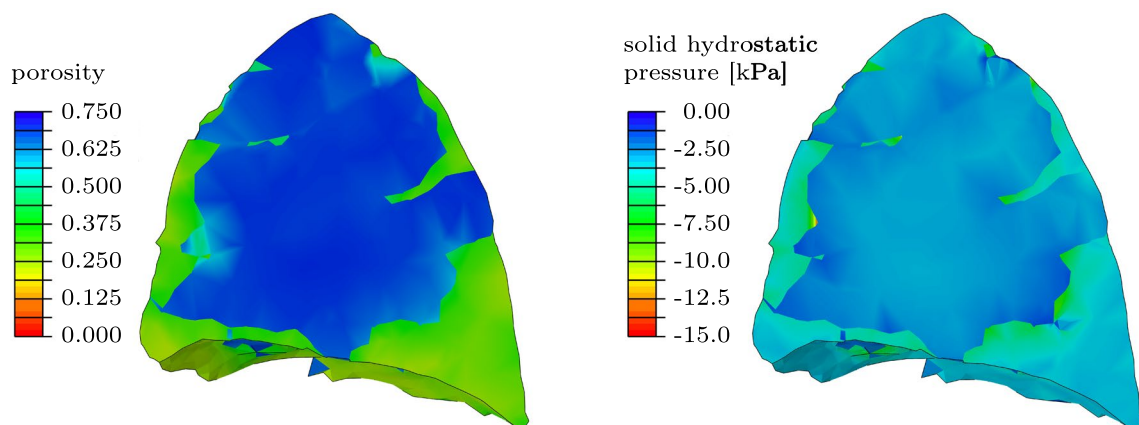

Fig. 5 Comparison of fluid fraction of the mixture (left) and the solid hydrostatic pressure [kPa] (right) in a sagittal slice of the lung for patient IPF1 in the case of a patient specific pleural pressure estimation (imposed $\overline{\alpha}_h$)

presented in Sect. 2.4. Results for both kinds of identification are shown in Fig. 3.

Compliance of the healthy lung region is higher than that of the diseased region except for the patient IPF2. This specificity is likely due to the very small amount of breathing between end-exhalation and end-inhalation images, resulting in a very small change in lung volume (around 14% while usually above 70%). These results are consistent with the literature reporting higher stiffness of fibrotic tissues (Plantier et al. 2018; Knudsen and Ochs 2018; Kang et al. 2021). As a reminder, normal compliance under natural breathing usually range from 0.6 to 1 L/kPa (Shelledy and Peters 2019), which is also consistent with our results.

The use of a non-patient specific pleural pressure systematically lead to estimate a lower compliance for the diseased region in comparison to the regional identification. Also, compliance estimation for patient IPF2 is more consistent since the small change in volume, due to clinical data, affects the value of the pleural pressure and no longer the stiffness of the lung tissues.

Note that patient COVID1 presents for both type of identification a larger compliance for the diseased region that the IPF patients, which might indicate an earlier stage of the disease.

3.2.2 Stress distribution

The assumption of a vicious mechanical circle has been formulated in the literature (Liu et al. 2010, 2015; Wu et al. 2020). This assumption states that mechanics may play a role in the evolution of pulmonary fibrosis and can be summarized as follows: a lower compliance of the diseased tissues leads to unphysiological stress concentrations that activate the production of collagen fibers inducing more fibrosis.

Figures 4 and 5 illustrate the local porosity and hydrostatic pressure distribution in the lung at end-inhalation for patient IPF1, in the case of estimation $p_{pl,i}$ imposed and $\overline{\alpha}_h$ imposed, respectively. The two regions considered as healthy and diseased can be distinguished looking at the porosity field, with a much lower fluid volume fraction of the mixture in the diseased area. The results clearly show an heterogeneous hydrostatic pressure field across the interface of the two regions, with stress concentrations in fibrotic tissues near healthy tissues that seem to support the mechanical vicious circle assumption. Moreover, one can observe a much more heterogeneous porosity field in the lung looking at results from estimation imposing $\overline{\alpha}_h$ in comparison to estimation imposing $p_{pl,i}$, with higher fluid volume fraction in the healthy region and lower in the diseased region. Thus, higher stress levels and stress concentrations across the interface can be observed in case of identification with imposed $\overline{\alpha}_h$.

4 Discussion

Personalized lung poromechanical modeling could represent an important tool for the better understanding of some of the mechanisms involved in pulmonary fibrosis. The patient-specific modeling pipeline presented in this study uses routine clinical images and aims to provide regional lung compliance in an automated way so that it can be run on large patients database. It builds upon (Patte et al. 2022), and the main pipelines improvements are summarized below:

- The segmentation and meshing steps were automated, as described in Sect. 2.3.1.
- Healthy and diseased regions are now explicitly represented in the mesh, with a coherent mesh interface, instead of a projected binary field, as described in Sect. 2.3.2.
- The image registration step was made more robust through a multi-level (rigid body, affine and full motion) decomposition, as described in Sect. 2.3.4.
- The parameter estimation step was made more consistent with a new parametrization of the optimization problem based on the estimation of a personalized pleural pressure in addition to material parameters, as described in Sect. 2.3.5.
- The entire model personalization pipeline was automated.

If global lung compliance is widely used by clinicians, regional lung compliance currently cannot be measured without the use of such tool. This additional personalized information about the patient could be helpful for further clinical decisions, quantify severity and evolution of the disease or evaluate the effectiveness of a treatment from a mechanical point of view.

In this study, poromechanical model of the lung was applied to three patients suffering from IPF and one from post-COVID-19 pulmonary fibrosis. We obtained results that are consistent with the current state of understanding of the disease. The parameters estimation systematically led to a stiffer diseased region in comparison to the healthy region, expect for patient IPF2 in the case where both lung regions stiffness where identified imposing the end-inhalation pleural pressure. This result highlights the very high sensitivity of this estimation to the quality of clinical data, since it is caused by the very small amount of breathing between end-exhalation and end-inhalation images. Imposing the stiffness of the healthy region, while the stiffness of the diseased region and the pleural pressure are estimated, gave the more consistent results. Indeed, for patient IPF2 the small amount of breathing led to the identification of a low pleural pressure instead of low tissue compliance. Moreover, the patient

specific pleural pressure estimation systematically led to lower compliance of the diseased region in comparison to the patient specific healthy region stiffness identification, as well as higher pleural pressure (except for patient IPF2). Compliance quantification should also be studied in relation to other clinical observations such as spirometry or carbon monoxide diffusing capacity and compared to reference values (Galetke et al. 2007).

Another interest of the poromechanical model is the study of the stress field in the lung tissues. Indeed, our model could help better understand the role of mechanics in pulmonary abnormal remodeling due to fibrosis. The existence of stress concentration at the border of the fibrotic region tends to confirm the hypothesis of the role of a mechanical vicious circle in the course of the disease. Results obtained from estimations using a patient specific pleural pressure give more heterogeneous porosity and stress fields in the lung that would still enforce the previous hypothesis. However, the model still needs to be applied on more patients, and longitudinally, in order to establish conclusive observations.

Thus, the pipeline automation presented in this study drastically reduces the need for manual intervention and offers the perspective to be used on large patients database of segmented lungs with healthy and diseased regions in further work. However, the computational cost is still high and the tool developed is complex to set up in an outsourcing context, such as in a radiology department. Thus, other methods are promising and should be explored. One can cite for instance methods of mechanical parameters identification based on full-field measurements and not requiring an actual resolution of the model (Avril et al. 2004, 2008), which could allow to compute regional lung compliances directly from finite element image registration without dealing with complex and still approximated boundary conditions. This reduction of modeling complexity would allow more robust and computationally efficient numerical simulations.

The present study has several limitations, both at the modeling and estimation levels, that are discussed in the following paragraphs. First, we considered a two-phases continuum, solid and fluid, were the solid phase regroups tissues and blood and the fluid phase corresponds to air. It would be possible to model three phases, considering for instance an independent but non patient-specific phase for blood. However, this rather simple representation allows the use of a poromechanical framework at the organ scale, taking into account heterogeneous porosity from personalized clinical data and projected onto the finite element mesh. One of the direct implication is that the measured porosity is not exactly represented but averaged inside an element. Moreover, we make the underlying assumption that the mechanical properties of the solid part of the mixture is homogeneous within one region of the mesh. A possible improvement could be the use of multi-scale model explicitly modeling lung interstitial tissues and airways (Álvarez-Barrientos et al. 2021).

Improving boundary conditions and loadings could also lead to more relevant model parameters estimation. Gravity, for instance, could be to taken into account, both on the tissue itself and the imposed pleural pressure. Indeed, effect of gravity on human lung deformation have been studied in for instance in Seyfi Noferest et al. (2018), and authors showed that gravitational effects are significant on lung deformation, especially in the top part of the lung that is far from the diaphragm, and tends to improve model accuracy. And in terms of boundary conditions, the modeling of organs in the mediastinum such as heart, vessels and trachea, constraining lungs displacements could improve the parameters estimation.

Furthermore, our model currently only represents two breathing states, namely end-exhalation & end-inhalation, considered in static equilibrium, and could be extended to dynamics to take into account inertia and hysteresis effects. However, patient-specific modeling always requires some trade-off between the model and clinically available data, and current computed tomography scans are very limited in terms of time frames. But recent magnetic resonance imaging techniques have allowed truly 4D imaging of the breathing lung (Boucneau et al. 2020), which could, once coupled to a dynamical poromechanics model, lead to more physiological personalized models.

Regarding the estimation pipeline itself, due to our personalized modeling approach – namely we do not use directly lung displacements that could be computed from image registration, but directly the images – the patients breathing kinematic is not perfectly reproduced in our modeling with the current boundary conditions, *i.e.*, homogeneous pleural pressure and thorax displacement extracted from the images. As already mentioned, one solution would be to use identification methods that consider directly the full-field kinematics extracted from the images (Avril et al. 2004, 2008). In the current setting, as already noted in Patte et al. (2022), the breathing motion error (*i.e.*, the distance between the motion predicted by the model and the one observed in the images), is better quantified when using a displacement-based cost function rather than an image-based cost function.

We assumed the existence of two regions in the lungs, considered as healthy and diseased, with homogeneous material properties. Note that, as mentioned above, the actual mechanical behavior within each region is still heterogeneous due to the heterogeneous porosity field. These regions are segmented using a method described in Rennotte et al. (2020) and explicitly meshed. The addition of several regions corresponding to specific CT visual analysis could be studied such as presence of ground-glass opacities, reticulations, honeycombing, *etc.* However, the

use of multiple regions would considerably increase the space of solutions of the inverse analysis process that may lead to non-uniqueness of the solution and increase the uncertainty of the quantification.

Since inverse problems are often ill-posed, we have limited our estimation to two parameters for each patient. An interesting outlook could be to perform uncertainty quantification when dealing with this small amount of input data with intrinsic noise. An interesting approach, based on a Bayesian multi-fidelity Monte-Carlo framework, has been recently proposed in the literature Nitzler et al. (2022).

Data availability The motion tracking tool is freely available at https://gitlab.inria.fr/mgenet/dolfin_warp. The computational mechanics tool is freely available at https://gitlab.inria.fr/mgenet/dolfin_mech. The images are available upon request.

Declarations

Ethical approval Patient data were retrospectively retrieved according to the French law on medical research and compiled as required by the *Commission Nationale de l'Informatique et des Libertés* (CNIL). The study not requiring an informed consent received authorization CLEA-2019-96 from the *Comité Local d'Éthique d'Avicenne* (CLEA).

Conflict of interest We declare no competing interests.

References

ABAQUS/Standard user's manual, Version 6.9. Dassault Systèmes Simulia Corp (2009)

Aln MS, Kehlet B, Logg A, Richardson C, Ring J, Rognes E, Wells GN (2015) The FEniCS project version 1(5):15

Arora H, Mitchell R, Johnston R, Manolesos M, Howells D, Sherwood J, Bodey A, Wanelik K (2021) Correlating local volumetric tissue strains with global lung mechanics measurements. Materials 14(2):439. https://doi.org/10.3390/ma14020439

Auger A, Hansen N (2005) A restart CMA evolution strategy with increasing population size. In: 2005 IEEE congress on evolutionary computation, vol. 2, pp. 1769–1776. IEEE. https://doi.org/10.1109/CEC.2005.1554902

Avilés-Rojas N, Hurtado DE Whole-lung finite-element models for mechanical ventilation and respiratory research applications 14. https://doi.org/10.3389/fphys.2022.984286

Avril S, Bonnet M, Bretelle A-S, Grédiac M, Hild F, Ienny P, Latourte F, Lemosse D, Pagano S, Pagnacco E, Pierron F (2008) Overview of identification methods of mechanical parameters based on full-field measurements. Exp Mech 48(4):381–402. https://doi.org/10.1007/s11340-008-9148-y

Avril S, Grédiac M, Pierron F (2004) Sensitivity of the virtual fields method to noisy data. Comput Mech 34(6):439–452. https://doi.org/10.1007/s00466-004-0589-6

Ballering AV, van Zon SKR, olde Hartman TC, Rosmalen JGM, (2022) Persistence of somatic symptoms after COVID-19 in the Netherlands: an observational cohort study. Lancet 400(10350):452–461. https://doi.org/10.1016/S0140-6736(22)01214-4

Berger L, Bordas R, Burrowes K, Grau V, Tavener S, Kay D (2016) A poroelastic model coupled to a fluid network with applications in lung modelling: a poroelastic model coupled to a fluid network with applications in lung modelling. Int J Numer Methods Biomed Eng. https://doi.org/10.1002/cnm.2731

Biot MA, Temple G (1972) Theory of finite deformations of porous solids. Indiana Univ Math J 21(7):597–620

Birzle AM, Hobrack SMK, Martin C, Uhlig S, Wall WA (2019) Constituent-specific material behavior of soft biological tissue: experimental quantification and numerical identification for lung parenchyma. Biomech Model Mechanobiol 18(5):1383–1400. https://doi.org/10.1007/s10237-019-01151-3

Birzle AM, Wall WA (2019) A viscoelastic nonlinear compressible material model of lung parenchyma - experiments and numerical identification. J Mech Behav Biomed Mater 94:164–175. https://doi.org/10.1016/j.jmbbm.2019.02.024

Boucneau T, Fernandez B, Larson P, Darrasse L, Maître X (2020) 3D Magnetic resonance spirometry. Sci Rep 10(1):9649. https://doi.org/10.1038/s41598-020-66202-7

Carloni A, Poletti V, Fermo L, Bellomo N, Chilosi M (2013) Heterogeneous distribution of mechanical stress in human lung: a mathematical approach to evaluate abnormal remodeling in IPF. J Theor Biol 332:136–140. https://doi.org/10.1016/j.jtbi.2013.04.038

Chapelle D, Gerbeau J-F, Sainte-Marie J, Vignon-Clementel IE (2010) A poroelastic model valid in large strains with applications to perfusion in cardiac modeling. Comput Mech 46(1):91–101. https://doi.org/10.1007/s00466-009-0452-x

Chapelle D, Moireau P (2014) General coupling of porous flows and hyperelastic formulations-from thermodynamics principles to energy balance and compatible time schemes. Eur J Mech B Fluids 46:82–96. https://doi.org/10.1016/j.euromechflu.2014.02.009

Concha F, Sarabia-Vallejos M, Hurtado DE (2018) Micromechanical model of lung parenchyma hyperelasticity. J Mech Phys Solids 112:126–144. https://doi.org/10.1016/j.jmps.2017.11.021

Cottin V, Crestani B, Valeyre D, Wallaert B, Cadranel J, Dalphin J-C, Delaval P, Israel-Biet D, Kessler R, Reynaud-Gaubert M, Aguilaniu B, Bouquillon B, Carre P, Danel C, Faivre J-B, Ferretti G, Just N, Kouzan S, Lebargy F, Marchand-Adam S, Philippe B, Prevot G, Stach B, Thivolet-Bejui F, Cordier J-F (2014) The French national reference centre and the network of competence centres for rare lung diseases: diagnosis and management of idiopathic pulmonary fibrosis: French practical guidelines. Eur Respir Rev 23(132):193–214. https://doi.org/10.1183/09059180.00001814

Fetita C, Tarando S, Brillet P-Y, Grenier PA (2016) Robust lung identification in MSCT via controlled flooding and shape constraints: dealing with anatomical and pathological specificity, p. 97881. https://doi.org/10.1117/12.2216687

Flaherty KR, Fell CD, Huggins JT, Nunes H, Sussman R, Valenzuela C, Petzinger U, Stauffer JL, Gilberg F, Bengus M, Wijsenbeek M (2018) Safety of nintedanib added to pirfenidone treatment for idiopathic pulmonary fibrosis. Eur Respir J 52(2):1800230. https://doi.org/10.1183/13993003.00230-2018

Galetke W, Feier C, Muth T, Ruehle K-H, Borsch-Galetke E, Randerath W (2007) Reference values for dynamic and static pulmonary compliance in men. Respir Med 101(8):1783–1789. https://doi.org/10.1016/j.rmed.2007.02.015

Genet M, Stoeck CT, von Deuster C, Lee LC, Kozerke S (2018) Equilibrated warping: finite element image registration with finite strain equilibrium gap regularization. Med Image Anal 50:1–22. https://doi.org/10.1016/j.media.2018.07.007

George PM, Wells AU, Jenkins RG (2020) Pulmonary fibrosis and COVID-19: the potential role for antifibrotic therapy. Lancet Respir Med 8(8):807–815. https://doi.org/10.1016/S2213-2600(20)30225-3

Giacomelli C, Piccarducci R, Marchetti L, Romei C, Martini C (2021) Pulmonary fibrosis from molecular mechanisms to therapeutic interventions: lessons from post-COVID-19 patients. Biochem Pharmacol 193:114812. https://doi.org/10.1016/j.bcp.2021.114812

Hansen N (2016) The CMA evolution strategy: A tutorial 1604.00772 [cs, stat]

Hartley PG, Galvin JR, Hunninghake GW, Merchant JA, Yagla SJ, Speakman SB, Schwartz DA (1994) High-resolution CT-derived measures of lung density are valid indexes of interstitial lung disease. J Appl Physiol 76(1):271–277. https://doi.org/10.1152/jappl.1994.76.1.271

Kang JH, Choi J, Chae KJ, Shin KM, Lee C-H, Guo J, Lin C-L, Hoffman EA, Lee C (2021) CT-derived 3D-diaphragm motion in emphysema and IPF compared to normal subjects. Sci Rep 11(1):14923. https://doi.org/10.1038/s41598-021-93980-5

Knudsen L, Ochs M (2018) The micromechanics of lung alveoli: structure and function of surfactant and tissue components. Histochem Cell Biol 150(6):661–676. https://doi.org/10.1007/s00418-018-1747-9

Lee LC, Genet M, Dang AB, Ge L, Guccione JM, Ratcliffe MB (2014) Applications of computational modeling in cardiac surgery. J Card Surg 29(3):293–302. https://doi.org/10.1111/jocs.12332.29citations(Crossref)[2022-04-27]

Leonard-Duke J, Evans S, Hannan RT, Barker TH, Bates JHT, Bonham CA, Moore BB, Kirschner DE, Peirce SM (2020) Multi-scale models of lung fibrosis. Matrix Biol 91–92:35–50. https://doi.org/10.1016/j.matbio.2020.04.003

Liu F, Lagares D, Choi KM, Stopfer L, Marinković A, Vrbanac V, Probst CK, Hiemer SE, Sisson TH, Horowitz JC, Rosas IO, Fredenburgh LE, Feghali-Bostwick C, Varelas X, Tager AM, Tschumperlin DJ (2015) Mechanosignaling through YAP and TAZ drives fibroblast activation and fibrosis. Am J Physiol-Lung Cell Mol Physiol 308(4):344–357. https://doi.org/10.1152/ajplung.00300.2014

Liu F, Mih JD, Shea BS, Kho AT, Sharif AS, Tager AM, Tschumperlin DJ (2010) Feedback amplification of fibrosis through matrix stiffening and COX-2 suppression. J Cell Biol 190(4):693–706. https://doi.org/10.1083/jcb.201004082

Maghsoudi-Ganjeh M, Mariano CA, Sattari S, Arora H, Eskandari M (2021) Developing a lung model in the age of COVID-19: a digital image correlation and inverse finite element analysis framework. Front Bioeng Biotechnol 9:684778. https://doi.org/10.3389/fbioe.2021.684778

Mariano CA, Sattari S, Quiros KAM, Nelson TM, Eskandari M (2022) Examining lung mechanical strains as influenced by breathing volumes and rates using experimental digital image correlation. Respir Res 23(1):92. https://doi.org/10.1186/s12931-022-01999-7

McGroder CF, Zhang D, Choudhury MA, Salvatore MM, D'Souza BM, Hoffman EA, Wei Y, Baldwin MR, Garcia CK (2021) Pulmonary fibrosis 4 months after COVID-19 is associated with severity of illness and blood leucocyte telomere length. Thorax 76(12):1242–1245. https://doi.org/10.1136/thoraxjnl-2021-217031

Michalski JE, Kurche JS, Schwartz DA (2022) From ARDS to pulmonary fibrosis: the next phase of the COVID-19 pandemic? Transl Res 241:13–24. https://doi.org/10.1016/j.trsl.2021.09.001

Morton SE, Dickson J, Chase JG, Docherty P, Desaive T, Howe SL, Shaw GM, Tawhai M (2018) A virtual patient model for mechanical ventilation. Comput Methods Programs Biomed 165:77–87

Neelakantan S, Xin Y, Gaver DP, Cereda M, Rizi R, Smith BJ, Avazmohammadi R (2022) Computational lung modelling in respiratory medicine. J R Soc Interface 19(191):20220062. https://doi.org/10.1098/rsif.2022.0062

Nitzler J, Biehler J, Fehn N, Koutsourelakis P-S, Wall WA (2022) A generalized probabilistic learning approach for multi-fidelity uncertainty quantification in complex physical simulations. arXiv. http://arxiv.org/abs/2001.02892

Nunes H, Schubel K, Piver D, Magois E, Feuillet S, Uzunhan Y, Carton Z, Tazi A, Levy P, Brillet P-Y, Nicholson AG, Kambouchner M, Valeyre D (2015) Nonspecific interstitial pneumonia: survival is influenced by the underlying cause. Eur Respir J 45(3):746–755. https://doi.org/10.1183/09031936.00148613

Patte C, Brillet P-Y, Fetita C, Bernaudin J-F, Gille T, Nunes H, Chapelle D, Genet M (2022) Estimation of regional pulmonary compliance in idiopathic pulmonary fibrosis based on personalized lung poromechanical modeling. J Biomech Eng 144(9):091008. https://doi.org/10.1115/1.4054106

Patte C, Genet M, Chapelle D (2022) A quasi-static poromechanical model of the lungs. Biomech Model Mechanobiol 21(2):527–551. https://doi.org/10.1007/s10237-021-01547-0

Plantier L, Cazes A, Dinh-Xuan A-T, Bancal C, Marchand-Adam S, Crestani B (2018) Physiology of the lung in idiopathic pulmonary fibrosis. Eur Respir Rev 27(147):170062. https://doi.org/10.1183/16000617.0062-2017

Project TC (2022) CGAL User and reference manual, 5.5 ed edn. CGAL Editorial Board. https://doc.cgal.org/5.5/Manual/packages.html

Rennotte S, Brillet P-Y, Fetita C (2020) Comparison of CNN architectures and training strategies for quantitative analysis of idiopathic interstitial pneumonia. In: Hahn HK, Mazurowski MA (eds.) Medical Imaging 2020: computer-aided diagnosis, vol. 11314, p. 113140. https://doi.org/10.1117/12.2548476

Ronneberger O, Fischer P, Brox T (2015) U-Net: convolutional networks for biomedical image segmentation. arXiv. http://arxiv.org/abs/1505.04597

Roth CJ, Ismail M, Yoshihara L, Wall WA (2017) A comprehensive computational human lung model incorporating inter-acinar dependencies: application to spontaneous breathing and mechanical ventilation. Int J Numer Method Biomed Eng 33(1):02787. https://doi.org/10.1002/cnm.2787

Sarabia-Vallejos MA, Zuñiga M, Hurtado DE (2019) The role of three-dimensionality and alveolar pressure in the distribution and amplification of alveolar stresses. Sci Rep 9(1):8783. https://doi.org/10.1038/s41598-019-45343-4

Schroeder W, Martin K, Lorensen B (2006) The visualization toolkit: an object-oriented Approach to 3D graphics ; visualize data in 3D - medical, engineering or scientific ; build your own applications with C++, Tcl, Java or Python ; Includes source sode for VTK (supports Unix, Windows and Mac), 4. ed edn. Kitware, Inc

Seyfi Noferest B, Santhanam AP, Ilegbusi OJ (2018) Effect of gravity on subject-specific human lung deformation. Math Comput Model Dyn Syst 24(1):87–101. https://doi.org/10.1080/13873954.2017.1382537

Shelledy DC, Peters JI (2019) Mechanical Ventilation, pp. 449–526. Jones & Bartlett Learning

Smith NP, de Vecchi A, McCormick M, Nordsletten DA, Camara O, Frangi AF, Delingette H, Sermesant M, Relan J, Ayache N, Krueger MW, Schulze WHW, Hose R, Valverde I, Beerbaum P, Staicu C, Siebes M, Spaan J, Hunter PJ, Weese J, Lehmann H, Chapelle D, Rezavi R (2011) EuHeart: personalized and integrated cardiac care using patient-specific cardiovascular modelling. Interface focus 1(3):349–64. https://doi.org/10.1098/rsfs.2010.0048.00070

Smith LN (2017) Cyclical learning rates for training neural networks. arXiv. http://arxiv.org/abs/1506.01186

Vishnevskiy V, Gass T, Szekely G, Tanner C, Goksel O (2017) Isotropic total variation regularization of displacements in parametric image registration. IEEE Trans Med Imaging 36(2):385–395. https://doi.org/10.1109/TMI.2016.2610583

Wall WA, Wiechert L, Comerford A, Rausch S (2010) Towards a comprehensive computational model for the respiratory system. Int J Numer Methods Biomed Eng. https://doi.org/10.1002/cnm.1378

Washko GR, Hunninghake GM, Fernandez IE, Nishino M, Okajima Y, Yamashiro T, Ross JC, Estépar RSJ, Lynch DA, Brehm JM, Andriole KP, Diaz AA, Khorasani R, D'Aco K, Sciurba FC, Silverman EK, Hatabu H, Rosas IO (2011) Lung volumes and emphysema in smokers with interstitial lung abnormalities. N Engl J Med 364(10):897–906. https://doi.org/10.1056/NEJMoa1007285

Wu H, Yu Y, Huang H, Hu Y, Fu S, Wang Z, Shi M, Zhao X, Yuan J, Li J, Yang X, Bin E, Wei D, Zhang H, Zhang J, Yang C, Cai T, Dai H, Chen J, Tang N (2020) Progressive pulmonary fibrosis is caused by elevated mechanical tension on alveolar stem cells. Cell 180(1):107–12117. https://doi.org/10.1016/j.cell.2019.11.027

Álvarez-Barrientos F, Hurtado DE, Genet M (2021) Pressure-driven micro-poro-mechanics: a variational framework for modeling the response of porous materials. Int J Eng Sci 169:103586. https://doi.org/10.1016/j.ijengsci.2021.103586